

Ultrafast energizing the parity-forbidden dark exciton in black phosphorus

Received: 10 January 2025

Accepted: 4 April 2025

Published online: 29 April 2025

 Check for updates

Guangzhen Shen^{1,2,6}, Xirui Tian^{1,2,6}, Limin Cao³, Hongli Guo⁴, Xintong Li^{1,2}, Yishu Tian^{1,2}, Xuefeng Cui^{1,2}, Min Feng³, Jin Zhao^{1,2}, Bing Wang^{1,2}, Hrvoje Petek⁵ & Shijing Tan^{1,2}

As conventional electronic materials approach their physical limits, the application of ultrafast optical fields to access transient states of matter captures imagination. The inversion symmetry governs the optical parity selection rule, differentiating between accessible and inaccessible states of matter. To circumvent parity-forbidden transitions, the common practice is to break the inversion symmetry by material design or external fields. Here we report how the application of femtosecond ultraviolet pulses can energize a parity-forbidden dark exciton state in black phosphorus while maintaining its intrinsic material symmetry. Unlike its conventional bandgap absorption in visible-to-infrared, femtosecond ultraviolet excitation turns on efficient Coulomb scattering, promoting carrier multiplication and electronic heating to ~3000 K, and consequently populating its parity-forbidden states. Interferometric time- and angle-resolved two-photon photoemission spectroscopy reveals dark exciton dynamics of black phosphorus on ~100 fs time scale and its anisotropic wavefunctions in energy-momentum space, illuminating its potential applications in optoelectronics and photochemistry under ultraviolet optical excitation.

Excitons in insulators and semiconductors¹ are the primary quasi-particles of light-matter interaction governed by quantum mechanical selection rules². Optical excitation creates a valence band (VB) hole and a conduction band (CB) electron that form an exciton state bound by the screened Coulomb interaction. Excitons are quanta that can transduce the energy and information of light, and define the optical-electrical-chemical properties of matter. When the VB and CB carry opposite spin or possess different momentum, optical transitions between them are forbidden, and their excitons are said to be dark^{3–5}. The suppressed radiative electron-hole recombination makes dark excitons longer-lived, attracting keen interest to switch them on at will^{6–9}. The parity of electronic wavefunctions, defined by switching (‘-’) or retention (‘+’) of sign upon point reflection, also defines the

strength of optical transitions. A striking example is the metastable excited state of helium, whose decay time to the same parity ground state is > 10⁶ longer than for the parity-allowed states¹⁰.

The optical selection rules require that the product of symmetry characters Γ is equal to one. The parity symmetry selection rule is satisfied when the electronic wave functions and light:

$$\Gamma_{VB} \otimes \Gamma_{CB} \otimes \Gamma_{photon} \otimes \Gamma_{exciton_envelope} = 1 \quad (1)$$

where the individual characters stand for VB and CB bands, photon, and exciton envelope^{11–14}. The component $\Gamma_{VB} \otimes \Gamma_{CB} \otimes \Gamma_{photon}$ symmetry determines the optical CB ← VB transitions, where $\Gamma_{photon} = -1$ restricts single-photon transitions to occur between electronic bands

¹Hefei National Research Center for Physical Sciences at the Microscale, New Cornerstone Science Laboratory, and Department of Physics, University of Science and Technology of China, Hefei, Anhui, China. ²Hefei National Laboratory, University of Science and Technology of China, Hefei, Anhui, China.

³School of Physics and Technology, Wuhan University, Wuhan, Hubei, China. ⁴School of Physics, Zhejiang University, Hangzhou, Zhejiang, China. ⁵Department of Physics and Astronomy and the IQ Initiative, University of Pittsburgh, Pittsburgh, Pennsylvania, USA. ⁶These authors contributed equally: Guangzhen Shen, Xirui Tian. ✉e-mail: zhaojin@ustc.edu.cn; bwang@ustc.edu.cn; petek@pitt.edu; tansj@ustc.edu.cn

of opposite parity¹¹. The exciton envelope parity is defined by the orbital angular momentum quantum number l as $\Gamma_{exciton_envelope} = (-1)^l$ (ref. 12,14), rendering the lowest-lying $1s$ exciton ground state of $\Gamma_{exciton_envelope} = 1$. Therefore, $1s$ exciton for one-photon $CB \leftarrow VB$ transitions between bands of opposite parity is bright (Fig. 1a), but dark when they have the same parity (Fig. 1b). The parity selection rule can be circumvented by breaking the inversion symmetry, as has been done by introducing lattice-distorting polarons in strongly confined perovskite quantum dots¹⁵ or distorting the electronic wave functions by external magnetic or electric fields in carbon nanotubes^{13,16,17}.

Here, we show how the parity-forbidden dark exciton state can be switched on in a bulk material even when its intrinsic crystal symmetry is maintained (Fig. 1c). BP is a particularly well-suited semiconductor^{18,19} for this study because (i) it has a direct band-gap²⁰ with remarkable optical responses²¹; (ii) its low atomic number²² gives it a negligible spin-orbit coupling; (iii) its excitonic wavefunctions express the highly anisotropic band dispersions in the Z-S (armchair, AC) and Z-T (zigzag, ZZ, Fig. 1d) directions²³; and (iv) its crystal structure exhibits multiple symmetries, providing an ideal platform to interrogate the optical selection rules (Supplementary Note 1). Especially, under three-dimensional space inversion, the CB2 as well as VB1-VB3 have even parity (ref. 21, Fig. 1d), making the $CB2 \leftarrow VB1$ -VB3 transitions strictly parity-forbidden (Supplementary Note 1.1). Previous research on BP with infrared excitation has focused on the allowed $CB1 \leftarrow VB1$ transition^{24,25} and its bright exciton^{26,27}. Herein we study by energy-momentum-time-resolved two-photon photoemission (2PP)

spectroscopy the high-lying parity-forbidden $CB2(e^-) \leftarrow VB1(h^+)$ dark exciton formation under femtosecond UV excitation.

Results

2PP spectral features of BP

Conventional angle-resolved photoemission spectra (ARPES) of BP excited with a He lamp reproduce the known^{18,20,21,28} anisotropic dispersions of the VB1-VB3 along the high-symmetry Z-T and Z-S lines (Fig. 1d and Supplementary Fig. 1). 2PP spectra excited with $\hbar\omega = 4.59$ eV femtosecond pulses record the electronic band structures of transiently populated CBs (Fig. 2a–c). Figure 2a shows the dispersions of CB2 and CB3 recorded in the 2PP $E(k_{\parallel})$ spectrum, for s -pol excitation with ZZ direction of BP aligned in the optical plane. Tuning the light polarization from s -pol ($\theta = 90^\circ$) to p -pol ($\theta = 0^\circ$) selectively probes different CBs and the free-electron dispersing image potential state (IPS)²⁹ (Fig. 2b,c). The observed band assignments are established by comparing the experimental and calculated band energies and masses (Supplementary Fig. 2), as summarized in Fig. 2d. Independent of the light polarization, the line traces taken at $k_{ZZ} = 0 \text{ \AA}^{-1}$ show that the 2PP signal rises from the surface work function (WF) edge of BP at $E_{final} = 4.68$ eV, and thereafter, gradually decreases to higher energies (right panel in Fig. 2a–c). The decreasing signal with E_{final} represents a hot thermal electron distribution within CB1. This suggests that the photoexcitation occurs by a Drude-like second-order inelastic scattering process³⁰ that populates all accessible CBs. At the intermediate $\theta = 60^\circ$ excitation polarization, an additional band appears ~ 85 meV

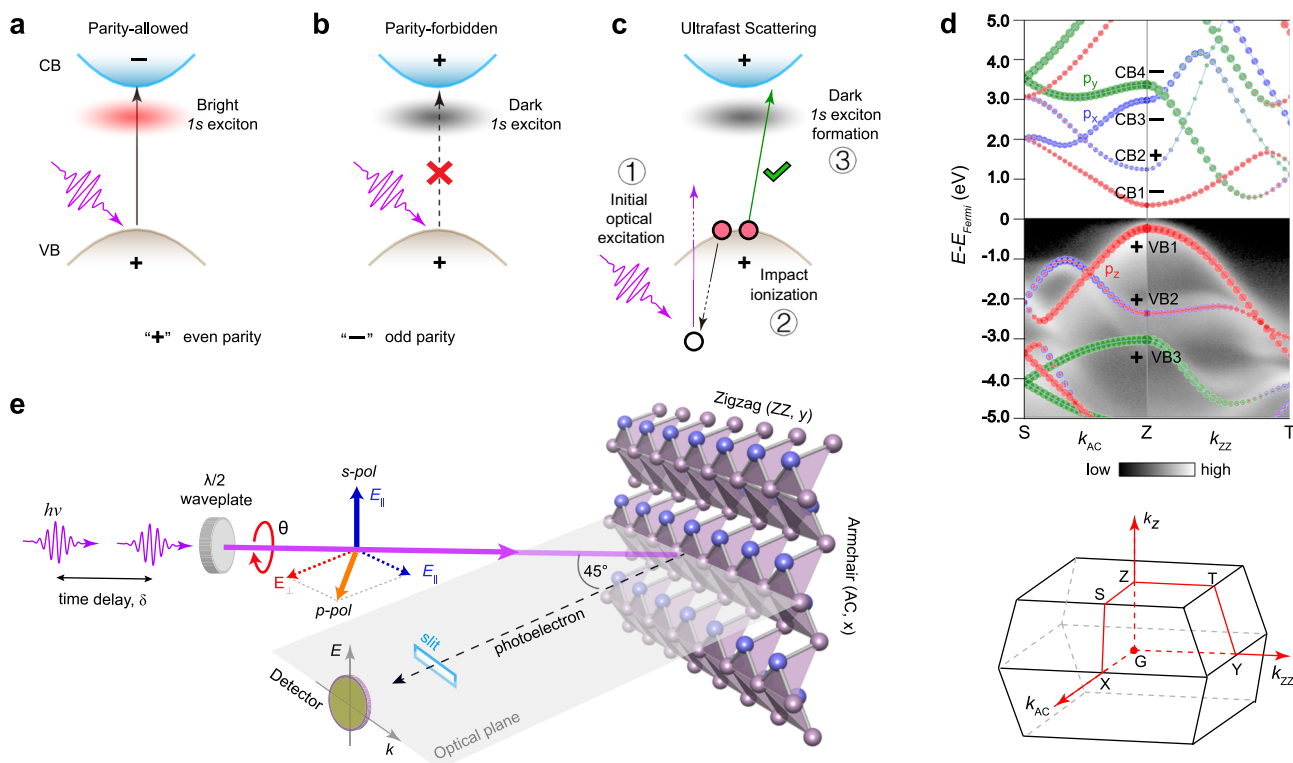


Fig. 1 | The optical excitation scheme of BP. **a, b** The schematic allowed opposite and forbidden same parity electric dipole transitions between VB and CB, which form bright (red shading) or dark (gray shading) $1s$ exciton state. **c** When the CB and VB have the same parity, the initial optical excitation generates a hot hole distribution ①, enabling ultrafast impact ionization within VBs to promote an electron to CB ②, turning on a dark exciton metastable state. Blue and Gray shadings in a–c indicate the CB and VB, respectively ③. **d** The calculated band structure of bulk BP with measured band dispersions along Z-S (k_{AC}) and Z-T (k_{ZZ}) lines [gray contrast is the ARPES spectrum measured with a He lamp ($\hbar\omega = 21.2$ eV)]. The 3D Brillouin zone is shown in the bottom. The colors and symbol sizes express the

dominant p_z (red), p_x (blue), and p_y (green) atomic orbital compositions of bands. Electrons in even symmetry VBs cannot be promoted to the same symmetry CBs by optical transitions. **e** Geometry of the optical excitation, the BP sample azimuth, and the photoelectron emission relative to the optical plane. The detector measures photoelectron counts as a function of energy and momentum parallel to the optical plane following excitation by two identical collinear pulses separated by time delay δ . A $\lambda/2$ waveplate defines the p -pol ($\theta = 0^\circ$) and s -pol ($\theta = 90^\circ$) field polarizations relative to the optical plane. Source data are provided as a Source Data file.

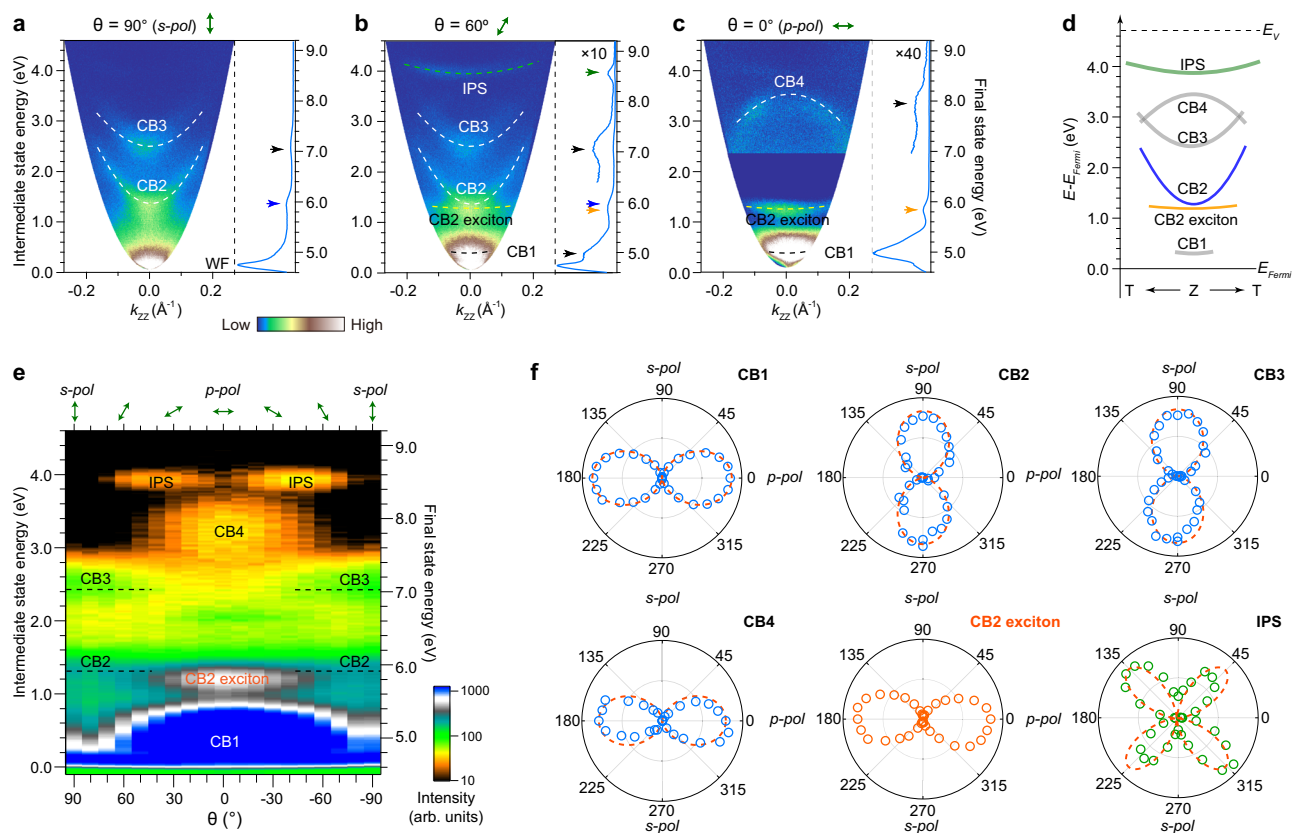


Fig. 2 | 2PP spectra of transiently populated electronic states in BP.

a–c. Representative 2PP $E(k_{||})$ spectra of BP excited with UV ($\hbar\omega = 4.59\text{eV}$) light polarized with $\theta = 90^\circ$ (*s-pol*), 60° , 0° (*p-pol*) with the ZZ azimuth in its optical plane. The left and right ordinates, respectively, numerate the intermediate state and final photoelectron energies (E_{int} and E_{final}), in the 2PP process, relative to the Fermi level (E_{Fermi}). The dashed curves guide the band dispersions. The right spectra are line profiles taken through $k_{zz} = 0 \text{ \AA}^{-1}$; the arrows point to the active bands in each spectrum. In (**b** and **c**), the higher energy range intensities are magnified to visualize

low-intensity spectral peaks. **d** Sketch of the observed CBs along k_{zz} with their specific dispersions. **e** A colormap composed of a series of line profiles taken at $k_{zz} = 0 \text{ \AA}^{-1}$ in 10° intervals for light polarization range from $\theta = -90^\circ$ to 90° ($s \rightarrow p \rightarrow s$). **f** Polar plots of the relative peak intensity of each state after background subtraction *vs.* the light polarization $\theta = 0^\circ$ to 360° . The red dashed lines show the calculated θ dependences of $|\text{TDMs}|^2$ for each $E_{\text{final}} \leftarrow \text{CBs}$ one-photon and the coherent $E_{\text{final}} \leftarrow \text{VB1}$ two-photon processes. Source data are provided as a Source Data file.

below the CB2 with flatter dispersion that cannot be assigned within the single-particle band structure of BP (Fig. 2b and Supplementary Fig. 3). Considering its binding relative to CB2, we attribute it to the CB2 exciton.

Assignments of the detected CB bands are affirmed by distinct polarization dependences of their 2PP spectra. As shown by the line profiles at $k_{zz} = 0 \text{ \AA}^{-1}$ taken by stepwise tuning of the $s \rightarrow p \rightarrow s$ excitation polarization (presented in the color map of Fig. 2e), the intensity maxima for CB1, CB4, and exciton state occur for *p-pol*, while for CB2 and CB3 they occur for *s-pol*. In polar coordinates, by comparing the relative 2PP intensity θ dependences with those of the calculated moduli square of transition dipole moments ($|\text{TDM}|^2$) for each CB (Fig. 2f and Supplementary Note 1.2), we conclude that the $\cos^2\theta$ dependence of CB1 and CB4, and the $\sin^2\theta$ dependence of CB2 and CB3 are defined by one-photon transitions from these transiently populated bands to the E_{final} photoemission continuum, in line with their incoherent population and subsequent photoemission. Further symmetry analysis of CBs explains their distinct polarization dependences. Specifically, when the ZZ azimuth of BP is aligned in the optical plane, the pseudospin symmetry is even for CB1 and CB4, and odd for CB2 and CB3, which defines their respective detection by *p-pol* and *s-pol* (Supplementary Note 1.3). By contrast, the IPS has intensity maxima at $\theta = \pm 45^\circ$, which stands out because photoemission from IPS is always maximum for normal emission. This, however, can be elegantly understood as a consequence of a coherent two-photon $E_{\text{final}} \leftarrow \text{IPS} \leftarrow \text{VB1}$ excitation that must have distinct $\sin^2\theta \cdot \cos^2\theta$

dependence (Supplementary Fig. 4). The CB2 exciton state appears for *p-pol*, because its joint electron-hole character of CB2 and VB1 both of odd symmetry, gives it a total even symmetry.

The anisotropic dark CB2(e⁻)←VB1(h⁺) exciton

We next establish the exciton state energy by tuning excitation $\hbar\omega = 3.94 - 4.77\text{eV}$ (Supplementary Fig. 5). Figure 3a records the E_{final} shift of each state with $\hbar\omega$, where the approximate fitted slopes of -1 confirm their incoherent population in the 2PP process, and determine the exciton binding energy of $E_b - 80 \pm 20 \text{ meV}$ relative to CB2 (Fig. 3b). Furthermore, 2PP recorded for ZZ to AC azimuths capture the anisotropies of CBs bands and CB2 exciton (the AC measurements are shown in Supplementary Figs. 6, 7 and analyzed in Supplementary Note 1.4). Surprisingly, the CB2 exciton dispersion reverses from positive along k_{zz} to negative along k_{AC} (Fig. 3c, d). A detailed description of the dispersion extraction in Supplementary Fig. 3, 7, gives the exciton effective masses $m_{\text{ex}}^*(ZZ) = 0.90 m_e$ and $m_{\text{ex}}^*(AC) = -0.36 m_e$ (m_e is the free electron mass).

We note that the true dispersion of an exciton is defined by the sum of the electron and hole masses³¹, whereas its photoemission spectra record the “apparent dispersion” from its photoemitted electron^{32–34}. Photoemission dissociates an exciton, with the energy and momentum conservation constraining its $E(k_{||})$ distribution by that remaining with the VB hole^{32–34}. Simulation of the “apparent dispersion” by the effective mass approximation model³⁴ shows that the effective exciton temperature, T_{ex} , can tune the “apparent dispersion”

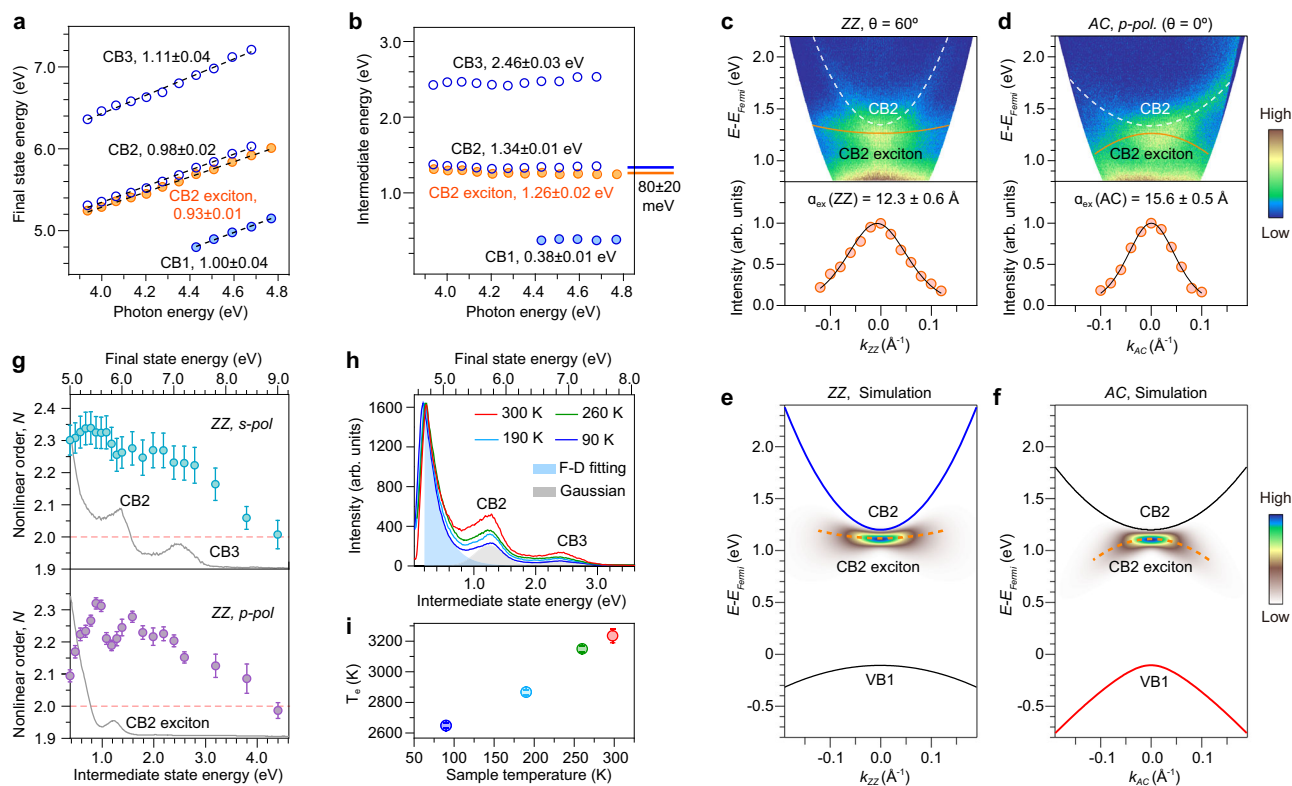


Fig. 3 | Anisotropic CB2 exciton in BP. **a** E_{final} values of CB1–CB3 and CB2 exciton *vs.* $\hbar\omega$, and their linear fitting (dashed lines), with numbers giving their slopes. The slopes of -1 signify that the 2PP experiment measures their incoherently excited populations. The data with hollow and solid circles are extracted from *s-pol* and *p-pol* 2PP spectra in Supplementary Fig. 5, respectively. **b** Data from **a** transformed to E_{int} to obtain the state energies (indicated by the numbers). The errors give the standard deviation. **c, d** 2PP spectra of CB2 excitons measured with $\hbar\omega = 4.59$ eV for the ZZ and AC azimuths, respectively. For ZZ, the polarization is set at $\theta = 60^\circ$ to record both the CB2 and CB2 exciton, while for AC, it is at $\theta = 0^\circ$. The measured dispersions of CB2 and CB2 exciton are indicated by white and orange curves, respectively. The lower panels show the k_{\parallel} momentum intensity distributions of CB2 excitons. The black curves indicate the fitting of the exciton wavefunction densities via $|\phi(k)|^2 = 1/[1 + (ka_{ex})^2/4]$ (ref. 32), reporting the anisotropic exciton

Bohr radii $a_{ex} = 12.3 \pm 0.6 \text{ \AA}$ (ZZ) and $15.6 \pm 0.5 \text{ \AA}$ (AC). **e, f** The simulated spectra of CB2(e^-) \leftarrow VB1(h^+) excitons along k_{ZZ} and k_{AC} , whose spectral dispersions are shown by the orange dashed curves. **g** The nonlinear order N obtained by fitting the *s-pol* (upper panel) and *p-pol* (lower panel) power-dependent 2PP spectral intensities (Supplementary Fig. 8) to $Y = I^N$, plotted *vs.* E_{int} (E_{final}). The gray line indicates the corresponding 2PP spectra excited with *s-pol* $\hbar\omega = 4.59$ eV. **h** 2PP spectra excited with *s-pol* $\hbar\omega = 4.43$ eV at BP sample temperatures of 300, 260, 190, and 90 K. The spectrum at 90 K shows Gaussian function fits for the CB2 and CB3 peaks (gray shading), and Fermi-Dirac (F-D) distribution for hot electrons giving $T_e = 2650 \pm 16 \text{ K}$ (blue shading). **i** The obtained hot electron T_e values plotted for different sample temperatures. The error bars in (**g**) and (**i**) are given by the 95% confidence interval for the nonlinear least-square parameter estimates. Source data are provided as a Source Data file.

to be close to VB dispersion at $T_{ex} \rightarrow 0$ and to CB dispersion at $T_{ex} \rightarrow \infty$ (Supplementary Note 2.1). The CB2 has a strong upward dispersion along k_{ZZ} , and the VB1 has a strong downward dispersion along k_{AC} (blue and red curves in Fig. 3e, f). This can generate the reverse “apparent dispersions” for CB2(e^-) \leftarrow VB1(h^+) exciton along k_{ZZ} and k_{AC} at a modest T_{ex} , where the experimentally observed dispersions are best simulated for $T_{ex} = 340 \text{ K}$ (color contrast in Fig. 3e, f). Furthermore, many-body perturbation theory calculation supports that the observed exciton is the $1s$ ground state of CB2(e^-) \leftarrow VB1(h^+) exciton with a calculated $E_b - 60$ meV and anisotropic wave function in real space (Supplementary Note 2.1).

Indirect excitation of CB2 and its exciton

As explained, parity forbids direct optical CB2 \leftarrow VB1 transitions, and therefore its $1s$ exciton is strictly a parity-forbidden dark state. So, elucidating excitation provides insight into the optical response of BP. The laser intensity (I) power-law²⁹ for photoelectron yield (Y) by two-photon absorption, $Y = I^N$, is expected to be $N = 2$. The measured $N > 2$ values below the highest energy photoelectron states, however, imply that there must be a carrier multiplication processes (Fig. 3g and Supplementary Fig. 8). This can occur by Auger-type scattering as it happens in copper^{35,36} and layered materials^{29,37}.

Like the quasi-two dimensional (2D) semimetal graphite²⁹, weak screening of the Coulomb interaction in the Van der Waals layered BP enables ultrafast electron excitation to CBs by second-order Coulomb scattering channels that are only restricted by energy and momentum conservation but not symmetry. This is immediately evident in the unstructured hot electron signal from CB1 in 2PP spectra of BP, whose intensity decreases above the WF edge following UV excitation. We attribute this signal to hot thermalized electrons with an effective electron temperature (T_e) given by the Fermi-Dirac (F-D) distribution, $f(E_{int}) = 1/[1 + \exp((E_{int} - E_{fermi})/k_B T_e)]$ (k_B is the Boltzmann constant). Fitting to the F-D distribution gives $T_e = 2650 - 3240 \text{ K}$ range for sample temperatures of 90–300 K (Fig. 3h, i). The effect of the sample temperature on the effective hot electron temperature implies that electron-phonon (*e-ph*) scattering also contributes to the hot electron generation and thermalization.

Ultrafast Auger-type scattering

Evidence for the delayed excitation of dark states and hot electron heating is conspicuous in the interferometric time-resolved 2PP measurements for excitation with a pair of identical, collinear, phase-correlated pump-probe pulses at $\hbar\omega = 4.02$ eV (Fig. 4). The

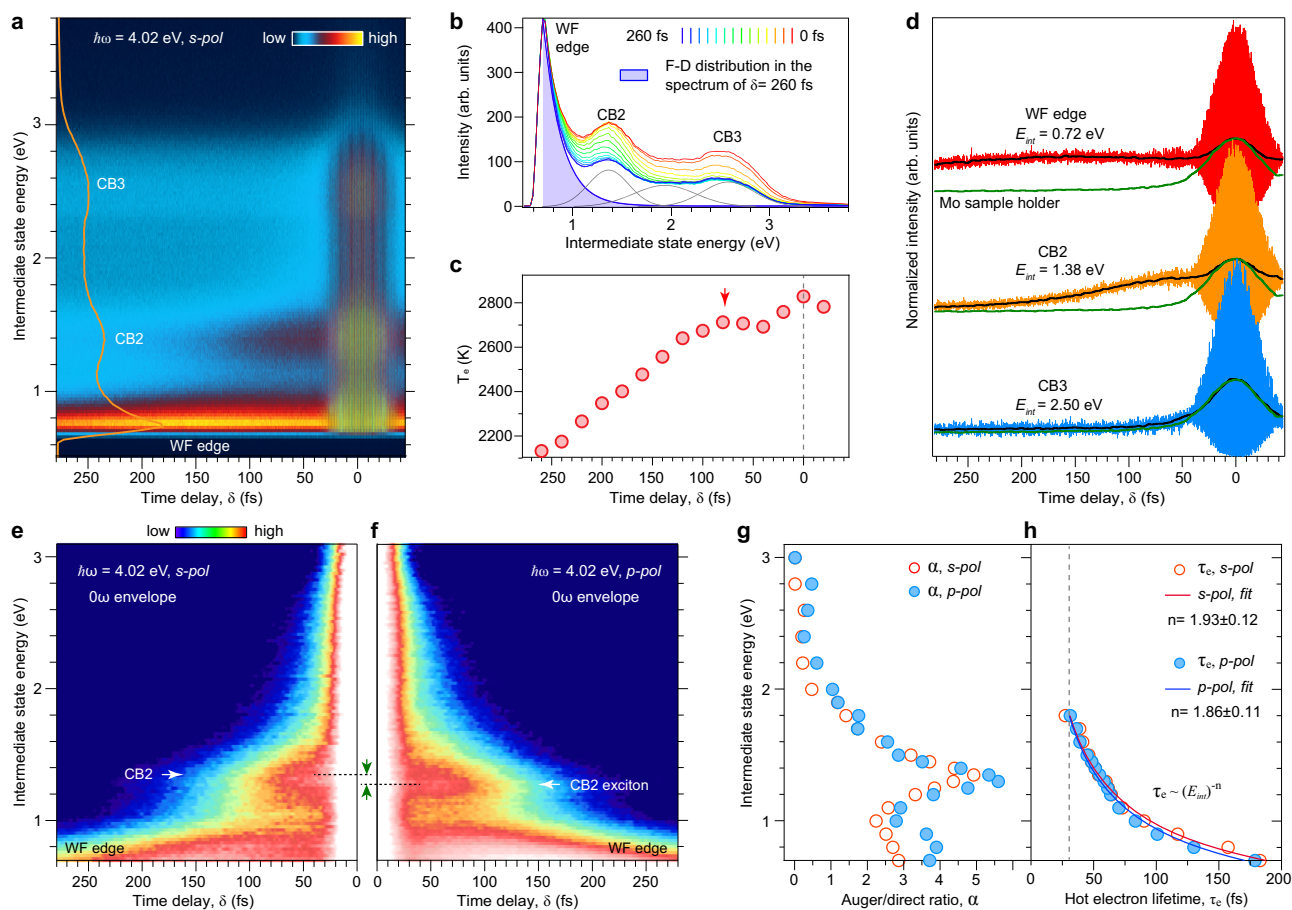


Fig. 4 | Time dependent population of CB2 and its exciton. **a** Interferometric time-resolved 2PP interferogram at $k_{ZZ} = 0 \text{ \AA}^{-1}$, displays the photoelectron counts (color scale) vs. E_{int} (ordinate) and δ (abscissa), excited by $s\text{-pol}$ $\hbar\omega = 4.02\text{eV}$ light (ZZ azimuth). The orange curve is a line profile at $\delta = 0\text{fs}$. **b** A series of vertical line profiles extracted from **a** taken in intervals of $\Delta\delta = 20\text{fs}$, and intensities normalized at WF edge. The spectrum at $\delta = 260\text{fs}$ is fitted by the F-D distribution (blue shaded; $T_e = 2130\text{K}$), and Gaussian lineshapes for the CB band peaks (gray). **c** nonmonotonically evolving T_e from F-D fitting of profiles with increasing δ in **(b)**. **d** Interferometric two-pulse correlation (I2PC) traces extracted as horizontal line profiles from **a** for E_{int} at the WF edge, CB2, and CB3, respectively, with intensities normalized at $\delta = 0\text{fs}$. The black curves are obtained by Fourier transformation of the I2PC data and reverse transformation of its zero-frequency 0ω component to

emphasize its slowly evolving hot electron signal. The green curve is the in situ pulse autocorrelation reference (Supplementary Fig. 9e, f). **e, f** Inverse Fourier transforms the map of the 0ω signal from the data in **a** for $s\text{-pol}$, and from the Supplementary Fig. 9c for $p\text{-pol}$ excitation; the intensities are normalized at $\delta = 0\text{fs}$. The transiently populated longer-lived dark CB2 and its exciton populations are evident **g, h** The delayed Auger/direct population ratio α and the hot electron lifetime τ_e from the OBE simulation of 0ω traces, plotted as a function of E_{int} , for $s\text{-pol}$ and $p\text{-pol}$ measurements. The vertical line in **(h)** indicates the limiting time resolution of $\sim 30\text{fs}$ (for $E_{\text{int}} > 1.8\text{eV}$, τ_e extraction is not reliable). In the $E_{\text{int}} = 0.7 - 1.8\text{eV}$ range, the data are fitted with $\tau_e \sim (E_{\text{int}})^{-n}$, giving $n = 1.93 \pm 0.12$ and 1.89 ± 0.11 for the $s\text{-pol}$ and $p\text{-pol}$ measurements, respectively. Source data are provided as a Source Data file.

measurements generate 3D movies of $E_{\text{int}}(k_{\parallel})$ vs. δ scanned in 0.064fs/frame steps to capture the coherent and incoherent electron dynamics with sub-optical-cycle accuracy (Supplementary Movies 1, 2). Extracting the $E_{\text{int}}(\delta)$ at $k_{\parallel} = 0 \text{ \AA}^{-1}$ from the movies generates 2D interferograms of the polarization and population dynamics for each state (Fig. 4a for $s\text{-pol}$ and Supplementary Fig. 9c for $p\text{-pol}$). With $s\text{-pol}$ excitation, the interferogram shows the main features of CB2 and CB3 superposed on the dominant hot electron signal with decreasing intensity above the WF edge in the vertical line trace at $\delta = 0\text{fs}$ (Fig. 4a). Plotting the vertical line traces at $\Delta\delta = 20\text{fs}$ intervals show the hot electron signal component to be decreasing (Fig. 4b). Fitting this component by F-D distribution (Fig. 4c) shows that $T_e(\delta)$ has the primary maximum at $\delta = 0\text{fs}$ where the laser fluence is maximum, and tellingly, a secondary maximum at $\delta = \sim 80\text{fs}$ (red arrow in Fig. 4c) where the hot electron population is multiplied and heated. We attribute the rising signal to retarded Auger-type scattering processes^{38–40}.

The contribution of the retarded carrier scattering is evident in the interferometric two-pulse correlation (I2PC, Fig. 4d) traces

obtained as horizontal line profiles through the interferogram in Fig. 4a, as well as the enhanced ($N > 2$) nonlinear order of 2PP signals in Fig. 3g. The phase-independent 0ω signal obtained by Fourier filtering⁴¹ of the I2PC scans records the incoherent electron dynamics (black traces in Fig. 4d). The 0ω trace for CB3 at $E_{\text{int}} = 2.5\text{eV}$ is almost identical to the reference pulse autocorrelation (green trace), because the electron dynamics at that energy are too fast to resolve. By contrast, the 0ω signals for CB2 and WF edge show a delayed rise and pedestal formation at $\delta > 50\text{fs}$, giving evidence for carrier multiplication^{35,36}. Plotting the 0ω traces at different E_{int} shows that the delayed rise feature primarily occurs at low E_{int} and becomes invisible at $E_{\text{int}} > 2.4\text{eV}$ (Supplementary Fig. 9b, d), indicating that the CB population by carrier multiplication decreases as E_{int} increases to reach the expected $N = 2$ for a two-photon process at $E_{\text{int}} = \hbar\omega$. Particularly, pronounced delayed rise signals appear at E_{int} of CB2 and CB2 exciton, as are evident in the 0ω maps under $s\text{-pol}$ and $p\text{-pol}$ light excitation (Fig. 4e, f). Moreover, the delayed rise features appear earlier under higher light fluence (Supplementary Fig. 10), as expected for the Auger-type scattering process⁴².

Optical Bloch equation (OBE) simulations at specific E_{int} including the delayed Auger-type generation, can well reproduce the 0ω traces (Supplementary Note 3), from which we can extract the hot electron lifetime τ_e ^{35,36}, and the ratio, α , of the delayed to the prompt hot electron population. As E_{int} increases from the WF edge, the value of α decreases non-monotonically (Fig. 4g), gaining secondary maxima at CB2 and CB2 exciton, signifying their dominant excitation is by carrier multiplication. The obtained τ_e is longest (~180 fs) at WF edge ($E_{\text{int}} = 0.7\text{eV}$) and decreases at higher E_{int} (Fig. 4h) with an approximate $\tau_e \sim (E_{\text{int}})^{-1.9}$ dependence, which is close to the inverse quadratic dependence of τ_e for e - e scattering in normal Fermi liquids⁴³. This invites a conclusion that for $E_{\text{int}} \geq 0.7\text{eV}$ above E_{Fermi} , e - e scattering dominates on the ~100 fs time scale, while closer to the CB minimum, the e - ph scattering may dominate on a longer time scale⁴³.

Discussion

The semiconducting BP with a layer thickness tunable bandgap presents a broad optical response in the visible-to-infrared range^{21,24} and attracts interest in its variable-spectrum optoelectronic applications⁴⁴. Its absorption in $\hbar\omega = 3 - 4\text{eV}$ UV range is regarded to have a “colossal”, five orders-of-magnitude, increase in photoconductivity relative to the visible-near-infrared excitation⁴⁵. Wu et al. attribute this changeover to the excitation of flat bands (G-Z direction) that may contribute a high density-of-states for excitation from -2 to 2eV ⁴⁵. Our femtosecond deep UV ($\hbar\omega = 4.68 - 3.94\text{eV}$) pulse 2PP spectroscopy of BP shows the photoexcitation unconventionally occurs through a second-order Drude-like process where transient e^-h^+ pairs turn on Coulomb interactions that activate carrier-carrier scattering that populates CB1-CB4, in sharp contrast to the conventional band-to-band transitions under visible excitation (Supplementary Note 4). Consequently, in the primary response, energy and momentum are conserved, generating the hot electron gas with T_e up to 3000 K in CB1 and populating CB2-CB4. The concomitantly generated hot holes participate in Auger-type interband carrier-carrier scattering. Particularly, VB1 electrons participate in impact ionization, where the energy of one recombining with a deep hole is transferred to the other to populate the CB2 to generate the parity-forbidden CB2(e^-) \leftarrow VB1(h^+) dark exciton state (Supplementary Fig. 11). The energy and momentum conservations in impact ionization determine the exciton distribution with finite center-of-mass (COM) momentum, thereby achieving the observed exciton temperature of $T_{\text{ex}} = 340\text{K}$ (Supplementary Fig. 15). Such unconventional optical response with exceptional dark exciton formation and hot electron generation extend the potential applications of BP in optoelectronics^{11,21,37,44} and photochemistry^{46,47} under femtosecond UV excitation.

The involvement of carrier scattering in UV absorption can be attributed to weak and time-dependent screening of the Coulomb interaction in 2D materials. The UV excited transient excitonic virtual e - h pairs scatter within the 30-fs excitation pulse window to generate real thermalized hot electrons and holes⁴⁸. The generated hot carrier plasma can undergo further carrier multiplication scattering on <100 fs time scale that is seen as the delayed dark state rise. This analysis is entirely consistent with the understanding that, while the electronic band structure picture of 2D materials is valid, the quasiparticle picture of their excitations is equivocal because of charge carrier Coulomb correlations that favor second-order scattering processes⁴⁸. Thus, our energy-momentum-time-resolved nonlinear 2PP spectroscopy shows that under femtosecond UV excitation, the optical response of 2D materials can deviate from band-to-band dipole transitions, opening new routes to access novel dark state with singular properties relative to the starting ground state. We expect that the departure from the quasiparticle concept under strong excitation is a general feature of 2D materials that show evidence of Coulomb correlations under weak excitation and low-temperature conditions⁴⁹.

Methods

Sample preparation

The single-crystalline BP samples are grown by the chemical vapor transport (CVT) method in a two-zone tube furnace using high-purity red phosphorus, tin iodide and tin powders as the starting materials⁵⁰. Commercial BP samples (HQ Graphene) are also used to check for the consistency of 2PP experiments. The BP surface is cleaved in situ under ultrahigh vacuum (UHV). A low-temperature scanning tunneling microscopy at constant current mode (STM, Omicron LT) is used to establish the surface cleanliness (Supplementary Fig. 1a)

2PP and 1PP measurements

A 1030 nm femtosecond laser (Light conversion, Pharos-20W) operating at a 500 kHz repetition pumps a self-built noncollinear optical parametric amplifier (NOPA) to produce tunable excitation pulse trains between 500–930 nm ($\hbar\omega_L = 2.48 - 1.33\text{eV}$) with an average output power of ~60–80 mW. The pulses are compressed by multiple reflections from a matched pair of negative dispersion mirrors to ~20–30 fs for further frequency doubling by a BBO crystal to 250–465 nm ($\hbar\omega = 4.96 - 2.67\text{eV}$). Dispersion compensation for UV pulses uses a series of four dispersive prisms to reach a pulse duration of ~30 fs. The laser beam is focused onto the sample at an incident angle of 45° from the surface normal with a spot diameter ~50 μm .

2PP measurements are carried out mainly at room temperature in a UHV chamber with a base pressure $< 1.5 \times 10^{-10}$ mBar. The manipulator can also cool the samples down to 90 K with liquid nitrogen, such as for the measurements in Supplementary Fig. 7 and 10, for a better signal-to-noise ratio. The 2PP spectra are collected with a hemispherical electron energy analyzer (Specs, Phoibos 150, $\pm 15^\circ$ acceptance angle). A 2D DLD delay-line detector (Surface Concept) records $E_{\text{final}}(k_{\parallel})$ values in single photoelectrons counting acquisition mode. A bias of 3 V is applied between the sample and the analyzer to collect low-energy photoelectrons. When $\hbar\omega < \text{WF}$, two-photon absorption excites electrons from below E_{Fermi} to above the vacuum level (E_v), to overcome the surface work function and undergo photoemission. The observed electron dynamics occur dominantly in bound intermediate states $E_{\text{int}}(k_{\parallel}) = E_{\text{final}}(k_{\parallel}) - \hbar\omega$. During the electronic system evolution, absorbing the second photon projects electrons into the photoemission continuum, where their energy and momentum are recorded.

As shown in Fig. 1e, the incident laser beam, the sample surface normal, and the analyzer slit are aligned in the optical plane. A $\lambda/2$ waveplate sets the excitation polarization between p - and s - pol . A 5-axis manipulator with in-plane azimuth rotation can align the ZZ or AC edges of BP crystals to the optical plane, where its crystalline orientations are further verified by recording the LEED pattern analysis (SPECS ErLEED 100, Supplementary Fig. 1b).

The conventional ARPES (referred to as 1PP) is excited by $\hbar\omega = 21.2\text{eV}$ from a He discharge lamp (VG Scienta, VUV5000). The optical excitation pathways for 1PP and 2PP are schematically shown in Supplementary Fig. 1f.

Interferometric time-resolved 2PP measurements

A Mach-Zehnder interferometer generates identical, collinear, phase-correlated pump-probe pulse pairs for time-resolved 2PP measurements³⁰. A piezoelectrically actuated translation stage scans the pump-probe time delay (δ), enabling the phase coherent response to be recorded with each frame recording 2D $E_{\text{int}}(k_{\parallel})$ images. Scanning the delay over $\delta = 280$ to -50 fs range in 64 attosecond steps records a 3D interferogram movie (Supplementary Movies 1, 2) of the variation of photoelectron counts in the energy-momentum-time domains^{41,51–56}. To improve the counting statistics, more than 200 pump-probe scans are accumulated together with the delay time calibration interference fringes at the laser center frequency. The calibration fringes define the

time axis with a constant optical cycle at specific excitation $\hbar\omega$. From the accumulated 3D interferogram movie, we extract the 2D interferograms of E_{int} vs. δ at specific $k_{||}$, such as in Fig. 4a and Supplementary Fig. 9.

Such interferograms are Fourier transformed (FT) from time to frequency domains to analyze responses at the dominant coherent polarization frequencies corresponding to $0\omega, 1\omega, 2\omega$ harmonics (ω is the laser frequency). For further analysis, 2D-FT spectra are inverse Fourier transformed back to the time domain, in particular, the 0ω phase-averaged component (Fig. 4e, f and Supplementary Fig. 10) is used for the analysis of optical phase-independent hot electron population dynamics. The OBE simulation details of the population dynamics are in Supplementary Note 3.

Calculations

Density functional theory (DFT) calculations are performed with the projector-augmented wave method (PAW)⁵⁷ as implemented in Vienna ab-initio simulation package (VASP)^{58,59}. The Perdew-Burke-Ernzerhof (PBE) functional⁶⁰ is used for the exchange-correlation potential. For geometry optimization, the vdW interaction is considered at the vdW-DF level with the optB88 exchange functional (optB88-vdW)^{61,62}. The plane wave cut-off energy is set as 400 eV. An $18 \times 18 \times 6$ k-mesh is used to sample the Brillouin zone. The atomic geometry is fully optimized until a residual force on each atom is less than 0.01 eV \AA^{-1} . Electronic band structure is calculated by hybrid functional (HSE06)⁶³ methods based on the atomic structures obtained from the full optimization by optB88-vdW, and the result is shown in Fig. 1d. Ab initio GW plus Bethe-Salpeter Equation (GW-BSE)^{64,65} calculations is performed using VASP as well to evaluate the exciton binding energy and wave function, with the same structure, energy cutoff and k-grid as in DFT calculation.

Data availability

The main data supporting the findings are provided in the Source data files with this paper. All the data that support the findings of this study are available from the corresponding author upon request. Source data are provided in this paper.

References

- Hopfield, J. J. Theory of the contribution of excitons to the complex dielectric constant of crystals. *Phys. Rev.* **112**, 1555–1567 (1958).
- Wang, G. et al. Colloquium: Excitons in atomically thin transition metal dichalcogenides. *Rev. Mod. Phys.* **90**, 021001 (2018).
- Jiang, X. et al. Real-time GW-BSE investigations on spin-valley exciton dynamics in monolayer transition metal dichalcogenide. *Sci. Adv.* **7**, eabf3759 (2021).
- Poem, E. et al. Accessing the dark exciton with light. *Nat. Phys.* **6**, 993–997 (2010).
- Loh, K. P. 2D materials: Brightening the dark excitons. *Nat. Nanotechnol.* **12**, 837–838 (2017).
- Zhou, Y. et al. Probing dark excitons in atomically thin semiconductors via near-field coupling to surface plasmon polaritons. *Nat. Nanotechnol.* **12**, 856–860 (2017).
- Zhang, X. X. et al. Magnetic brightening and control of dark excitons in monolayer WSe₂. *Nat. Nanotechnol.* **12**, 883–888 (2017).
- Madeo, J. et al. Directly visualizing the momentum-forbidden dark excitons and their dynamics in atomically thin semiconductors. *Science* **370**, 1199–1204 (2020).
- Schmitt, D. et al. Formation of moire interlayer excitons in space and time. *Nature* **608**, 499–503 (2022).
- Hodgman, S. S. et al. Metastable Helium: A New Determination of the Longest Atomic Excited-State Lifetime. *Phys. Rev. Lett.* **103**, 053002 (2009).
- Ye, Z. et al. Probing excitonic dark states in single-layer tungsten disulphide. *Nature* **513**, 214–218 (2014).
- Kazimierzczuk, T., Frohlich, D., Scheel, S., Stolz, H. & Bayer, M. Giant Rydberg excitons in the copper oxide Cu₂O. *Nature* **514**, 343–347 (2014).
- Matsunaga, R., Matsuda, K. & Kanemitsu, Y. Evidence for dark excitons in a single carbon nanotube due to the aharonov-Bohm effect. *Phys. Rev. Lett.* **101**, 147404 (2008).
- Orfanakis, K. et al. Rydberg exciton-polaritons in a Cu₂O microcavity. *Nat. Mater.* **21**, 767–772 (2022).
- Rossi, D. et al. Light-induced activation of forbidden exciton transition in strongly confined perovskite quantum dots. *ACS Nano*. **12**, 12436–12443 (2018).
- Uda, T., Yoshida, M., Ishii, A. & Kato, Y. K. Electric-field induced activation of dark excitonic states in carbon Nanotubes. *Nano Lett.* **16**, 2278–2282 (2016).
- Ishii, A., Machiya, H. & Kato, Y. K. High efficiency dark-to-bright exciton conversion in carbon nanotubes. *Phys. Rev. X* **9**, 041048 (2019).
- Li, L. et al. Black phosphorus field-effect transistors. *Nat. Nanotechnol.* **9**, 372–377 (2014).
- Qiao, J., Kong, X., Hu, Z.-X., Yang, F. & Ji, W. High-mobility transport anisotropy and linear dichroism in few-layer black phosphorus. *Nat. Commun.* **5**, 4475 (2014).
- Kim, J. et al. Observation of tunable band gap and anisotropic Dirac semimetal state in black phosphorus. *Science* **349**, 723–726 (2015).
- Yuan, H. et al. Polarization-sensitive broadband photodetector using a black phosphorus vertical p-n junction. *Nat. Nanotechnol.* **10**, 707–713 (2015).
- Kurpas, M., Gmitra, M. & Fabian, J. Spin properties of black phosphorus and phosphorene, and their prospects for spin calorics. *J. Phys. D Appl. Phys.* **51**, 174001 (2018).
- Tran, V., Soklaski, R., Liang, Y. & Yang, L. Layer-controlled band gap and anisotropic excitons in few-layer black phosphorus. *Phys. Rev. B* **89**, 235319 (2014).
- Zhou, S. et al. Pseudospin-selective Floquet band engineering in black phosphorus. *Nature* **614**, 75–80 (2023).
- Chen, Z. et al. Band Gap Renormalization, Carrier multiplication, and stark broadening in Photoexcited Black Phosphorus. *Nano Lett.* **19**, 488–493 (2019).
- Wang, X. et al. Highly anisotropic and robust excitons in monolayer black phosphorus. *Nat. Nanotechnol.* **10**, 517–521 (2015).
- Zhang, G. et al. Determination of layer-dependent exciton binding energies in few-layer black phosphorus. *Sci. Adv.* **4**, eaap9977 (2018).
- Jung, S. W. et al. Black phosphorus as a bipolar pseudospin semiconductor. *Nat. Mater.* **19**, 277–281 (2020).
- Tan, S., Argondizzo, A., Wang, C., Cui, X. & Petek, H. Ultrafast Multiphoton Thermionic Photoemission from Graphite. *Phys. Rev. X* **7**, 011004 (2017).
- Petek, H. & Ogawa, S. Femtosecond time-resolved two-photon photoemission studies of electron dynamics in metals. *Prog. Surf. Sci.* **56**, 239–310 (1997).
- Mattis, D. C. & Gallinar, J. P. What is the Mass of an Exciton? *Phys. Rev. Lett.* **53**, 1391–1393 (1984).
- Fukutani, K. et al. Detecting photoelectrons from spontaneously formed excitons. *Nat. Phys.* **17**, 1024–1030 (2021).
- Man, M. K. L. et al. Experimental measurement of the intrinsic excitonic wave function. *Sci. Adv.* **7**, eaag0192 (2021).
- Rustagi, A. & Kemper, A. F. Photoemission signature of excitons. *Phys. Rev. B* **97**, 235310 (2018).
- Petek, H., Nagano, H., Weida, M. J. & Ogawa, S. The role of Auger decay in hot electron excitation in copper. *Chem. Phys.* **251**, 71–86 (2000).

36. Petek, H., Nagano, H. & Ogawa, S. Hot-electron dynamics in copper revisited: The d-band effect. *Appl. Phys. B* **68**, 369–375 (1999).
37. Lin, K.-Q. et al. High-lying valley-polarized trions in 2D semiconductors. *Nat. Commun.* **13**, 6980 (2022).
38. Klimov, V. I. Multicarrier interactions in Semiconductor Nanocrystals in Relation to the Phenomena of Auger Recombination and Carrier Multiplication. *Annu. Rev. Condens. Matter Phys.* **5**, 285–316 (2014).
39. Fu, J. et al. Hot carrier cooling mechanisms in halide perovskites. *Nat. Commun.* **8**, 1300 (2017).
40. Paul, K. K., Kim, J.-H. & Lee, Y. H. Hot carrier photovoltaics in van der Waals heterostructures. *Nat. Rev. Phys.* **3**, 178–192 (2021).
41. Reutzler, M., Li, A. & Petek, H. Coherent two-dimensional multi-photon photoelectron Spectroscopy of Metal Surfaces. *Phys. Rev. X* **9**, 011044 (2019).
42. Zhang, T. et al. Regulation of the luminescence mechanism of two-dimensional tin halide perovskites. *Nat. Commun.* **13**, 60 (2022).
43. Bauer, M., Marienfeld, A. & Aeschlimann, M. Hot electron lifetimes in metals probed by time-resolved two-photon photoemission. *Prog. Surf. Sci.* **90**, 319–376 (2015).
44. Kim, H. et al. Actively variable-spectrum optoelectronics with black phosphorus. *Nature* **596**, 232–237 (2021).
45. Wu, J. et al. Colossal ultraviolet photoresponsivity of few-layer black phosphorus. *ACS Nano* **9**, 8070–8077 (2015).
46. Zhang, K. et al. Black phosphorene as a hole extraction layer boosting solar water splitting of oxygen evolution catalysts. *Nat. Commun.* **10**, 2001 (2019).
47. Kalay, E., Küçükkeçeci, H., Kilic, H. & Metin, Ö. Black phosphorus as a metal-free, visible-light-active heterogeneous photoredox catalyst for the direct C–H arylation of heteroarenes. *Chem. Commun.* **56**, 5901–5904 (2020).
48. Tomadin, A., Brida, D., Cerullo, G., Ferrari, A. C. & Polini, M. Nonequilibrium dynamics of photoexcited electrons in graphene: Collisional scattering, Auger processes, and the impact of screening. *Phys. Rev. B* **88**, 035430 (2013).
49. Rodin, A., Trushin, M., Carvalho, A. & Castro Neto, A. H. Collective excitations in 2D materials. *Nat. Rev. Phys.* **2**, 524–537 (2020).
50. Cui, X. et al. Realizing nearly-free-electron like conduction band in a molecular film through mediating intermolecular van der Waals interactions. *Nat. Commun.* **10**, 3374 (2019).
51. Cui, X. et al. Transient excitons at metal surfaces. *Nat. Phys.* **10**, 505–509 (2014).
52. Tan, S. et al. Plasmonic coupling at a metal/semiconductor interface. *Nat. Photonics* **11**, 806–812 (2017).
53. Tan, S. et al. Coherent electron transfer at the Ag/graphite heterojunction interface. *Phys. Rev. Lett.* **120**, 126801 (2018).
54. Reutzler, M., Li, A., Wang, Z. & Petek, H. Coherent multidimensional photoelectron spectroscopy of ultrafast quasiparticle dressing by light. *Nat. Commun.* **11**, 2230 (2020).
55. Li, A. et al. Towards full surface Brillouin zone mapping by coherent multi-photon photoemission. *N. J. Phys.* **22**, 073035 (2020).
56. Petek, H., Li, A., Li, X., Tan, S. & Reutzler, M. Plasmonic decay into hot electrons in silver. *Prog. Surf. Sci.* **98**, 100707 (2023).
57. Blöchl, P. E. Projector augmented-wave method. *Phys. Rev. B* **50**, 17953 (1994).
58. Kresse, G. & Furthmüller, J. Efficient iterative schemes for ab initio total-energy calculations using a plane-wave basis set. *Phys. Rev. B* **54**, 11169 (1996).
59. Kresse, G. & Furthmüller, J. Efficiency of ab-initio total energy calculations for metals and semiconductors using a plane-wave basis set. *Comput. Mater. Sci.* **6**, 15–50 (1996).
60. Perdew, J. P., Burke, K. & Ernzerhof, M. Generalized gradient approximation made simple. *Phys. Rev. Lett.* **77**, 3865 (1996).
61. Klimeš, J., Bowler, D. R. & Michaelides, A. Van der Waals density functionals applied to solids. *Phys. Rev. B* **83**, 195131 (2011).
62. Klimeš, J., Bowler, D. R. & Michaelides, A. Chemical accuracy for the van der Waals density functional. *J. Phys. Condens. Matter* **22**, 022201 (2009).
63. Heyd, J., Scuseria, G. E. & Ernzerhof, M. Hybrid functionals based on a screened Coulomb potential. *J. Chem. Phys.* **118**, 8207–8215 (2003).
64. Hybertsen, M. S. & Louie, S. G. Electron correlation in semiconductors and insulators: band gaps and quasiparticle energies. *Phys. Rev. B* **34**, 5390–5413 (1986).
65. Rohlfing, M. & Louie, S. G. Electron-hole excitations and optical spectra from first principles. *Phys. Rev. B* **62**, 4927–4944 (2000).

Acknowledgements

S.T. acknowledges the CAS Project for Young Scientists in Basic Research (YSBR-054). B.W. acknowledges the New Cornerstone Science Foundation. H.P. acknowledges the NSF grant CHE-2102601 and CHE-1414466, as well as the President's International Fellowship Initiative of CAS. We also appreciate the support from the Innovation Program for Quantum Science and Technology (2021ZD0303302), CAS Strategic Priority Research Program (XDB36020200), and the National Natural Science Foundation of China (22425206, 11904349, 12125408).

Author contributions

This is joint research conducted at the University of Science and Technology of China (USTC), the University of Pittsburgh (Pitt), and Wuhan University (WHU). S.T. and H.P. initiated the research at Pitt; S.T. and B.W. supervised the experiments at USTC; M.F. and L.C. supervised the synthesis of BP crystals at WHU; J.Z. supervised the calculations at USTC. G.S. and S.T. performed the 2PP experiments, processed and analyzed the data, prepared the figures, and wrote the first draft of the manuscript; X.T. and H.G. performed the calculations; X.C., X.L., and Y.T. participated in the construction of the 2PP experimental setup; H.P. and S.T. provided the interpretation of ultrafast Auger scattering and finalized the manuscript; all authors contributed to the discussion.

Competing interests

The authors declare no competing interests.

Additional information

Supplementary information The online version contains supplementary material available at <https://doi.org/10.1038/s41467-025-58930-z>.

Correspondence and requests for materials should be addressed to Jin Zhao, Bing Wang, Hrvoje Petek or Shijing Tan.

Peer review information *Nature Communications* thanks the anonymous reviewer(s) for their contribution to the peer review of this work. A peer review file is available.

Reprints and permissions information is available at <http://www.nature.com/reprints>

Publisher's note Springer Nature remains neutral with regard to jurisdictional claims in published maps and institutional affiliations.

Open Access This article is licensed under a Creative Commons Attribution-NonCommercial-NoDerivatives 4.0 International License, which permits any non-commercial use, sharing, distribution and reproduction in any medium or format, as long as you give appropriate credit to the original author(s) and the source, provide a link to the Creative Commons licence, and indicate if you modified the licensed material. You do not have permission under this licence to share adapted material derived from this article or parts of it. The images or other third party material in this article are included in the article's Creative Commons licence, unless indicated otherwise in a credit line to the material. If material is not included in the article's Creative Commons licence and your intended use is not permitted by statutory regulation or exceeds the permitted use, you will need to obtain permission directly from the copyright holder. To view a copy of this licence, visit <http://creativecommons.org/licenses/by-nc-nd/4.0/>.

© The Author(s) 2025